Supplementary Information

Insights into the nature of Cu doping in amorphous mesoporous alumina

Liangjie Fu, Xiaoyu Li, Mingzhu Liu, Huaming Yang[*]

Department of Inorganic Materials, School of Resources Processing and Bioengineering, Central South University,
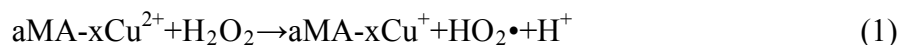
Changsha 410083, China

[*] *Corresponding author. Tel: +86-731-88830549; Fax: +86-731-88710804.*

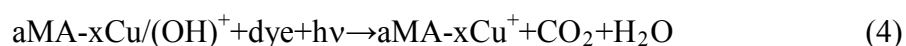*E-mail address: hmyang@csu.edu.cn (H. Yang).*

1. Photocatalytic properties

Since no visible-light decolorization is observed, we then focused on the photocatalystic reaction under UV irradiation. The reaction system, with the presence of both UV irradiation and hydrogen peroxide, is known as the photo-Fenton-like reaction if Metal ions other than Fe are used [1]. After several times of recycle use, the color of aMA-xCu changed from blue to green, to brown, similar to the Cu/ZSM case [2], indicating the reduction of Cu^{2+} to Cu^+. The reoxidation of reduced metal ions by HO• or holes will lower the photocatalytic properties [3]. Fenton and photo-Fenton processes are highly pH dependent. Under acidic pH condition, the MO transformed to MO^*, which is more easily degraded, due to the lowered redox potential, increasing the photodegradation rate. Hence, while •OH functions as the primary oxidant in the Fenton reagent-induced organic oxidation, the degradation effect of Cu becomes more significant at low pH. Lewis acid sites can attract electron

1

density from Cu to alumina and thus raise the oxidation potential of the Cu center [4]. The presence of

Lewis acid sites in aMA-xCu facilitated the reduction Cu^{2+} to Cu^{+} by H_2O_2. The enhanced reduction

ability of Cu increased the degradation rate of MO dyes by following reaction:

$$aMA\text{-}xCu^{2+}+H_2O_2 \rightarrow aMA\text{-}xCu^{+}+HO_2 \bullet + H^{+} \tag{1}$$

$$aMA\text{-}xCu^{2+}+HO_2 \bullet + H^{+} \rightarrow aMA\text{-}xCu^{+}+\bullet OH + OH^{-} \tag{2}$$

While the valence band edge is lower than the redox potential of the aqueous solution, the holes

generated from excitation can easily be transferred to degrade the MO dyes via following reaction:

$$aMA\text{-}xCu^{2+}+H_2O_2 \rightarrow aMA\text{-}xCu/(OH)^{+}+OH^{-} \tag{3}$$

$$aMA\text{-}xCu/(OH)^{+}+dye+h\nu \rightarrow aMA\text{-}xCu^{+}+CO_2+H_2O \tag{4}$$

On the other hand, the reduced recombination rate of photogenerated hole−electron pairs might be

due to the transition of photogenerated electrons from conduction band of aMA-xCu to localized

metal 3d orbital and the increased amount of oxygen vacancies when Cu atoms were doped

into aMA-xCu. Based on DFT calculations, the low potential of CBM of aMA-xCu limited the

separation of photogenerated hole−electron pairs, which inhibited the quantum yield.

2. Building of amorphous alumina models (tetragonal distorted structure with oxygen deficiency)

In real case, there are many amorphous alumina structures, and the modeling of amorphous Al_2O_3

is still in debate, for which oxygen deficient model and tetragonal distorted model has been proposed

decades ago.[5] Since Karl Josef Bayer introduced his elegant process for the industrial production of

aluminum oxide a hundred years ago, progress is still being made for this material. Two decades ago,

the oxides and hydroxides of alumina are systematically reviewed by Wefers.[5] In the pioneer work about the kinetic and mechanism of alumina phase transition,[6] Dignam et al. proposed that the γ-Al_2O_3 crystallites grow as a result of transport of oxygen species through the amorphous film. Recently, Perevalov et al. confirmed that oxygen vacancies have similar characters in crystalline γ-Al_2O_3 and amorphous Al_2O_3.[7]

Actually, amorphous alumina has been usually derived from dehydration of aluminum hydroxides, or mechanochemical processing. And, as we know, in the former case the 5-coordinated Al atom Al(V) number is influenced by the detailed dehydration process, depending on the synthesis process (e.g., higher calcination temperature leading to fast dehydration, would cause less dispersed or diminished Al(V) distribution.). In the later case, the mechanochemical processing (high-energy grinding) can not only disrupt the long-range atomic order of crystal but also make crystal nanoparticles amorphousized, in which case the Al(V) arise from the movement of O from octahedral to tetrahedral sites with the creation of oxygen anion vacancies adjacent to occupied octahedral sites.

It was well known that most of the amorphous Al_2O_3 structures were generated from molecular dynamics (MD) calculations using the transferable empirical pair potentials [8–11], which was effective for the structure estimation of metal oxides with accurate coordination number. The Al coordination number increased with the increase of the density [8,9], which could be related to an amorphous-amorphous phase transition under higher temperature [12,13]. However, none of these MD results gave the ratio of four-, five-, six-coordinated Al atoms as observed from the NMR results of the as-synthesized mesoporous alumina (Fig. 1c). Here, we have generated the amorphous phase

directly from the ordered crystal phase, both oxygen deficient model and tetragonal distorted model were studied. A detailed analysis of the difference between real structure and our amorphous atomic structure was first performed. The calculated formation entropy for oxygen deficient model is several eV higher than the tetragonal distorted model. Hence, from energy point of view, the tetragonal distorted model was chosen as the amorphous model in this study, and expected to give a better description for the as-synthesized mesoporous alumina.

In this work, as for the mesoporous amorphous system studied here, we have generated the amorphous phase from the ordered crystal model (the spinel gamma alumina model [7]) by distorting the local structure of gamma alumina lattice. We have tried to maximize the degree of distortion by randomly displacing both the Al and O atoms, and the final structure relaxed is obtained by displacing the four-coordinated oxygen to the middle region (ie, interstial site) of two nearby AlO_4 tetrahedra. The oxygen migrated and bonded to the nearby AlO_4 tetrahedra, left an oxygen vacancy at the former site, which altered three adjacent six-coordinated Al to five-coordinated Al, and formed several distorted five-coordinated structures. The degree of distortion is further increased in such a way until the ratio of Al(Td)/Al(V)/Al(Oh) coordination is agreement with experimental observation. The simulated ratio of Al(Td)/Al(V)/Al(Oh) is approximately 25%/50%/25% in this model, in well agreement with our experimental NMR results. The density is in agreement with previous report [8–11]. Furthermore, one benefit of this model for mesoporous alumina is that the amount of Al(V) in this model can be tailored by introducing further distortions using the similar movement described above to simulate the diverse mesoporous alumina structures as observed from experimental NMR results.[12]

In fact, the combination of Al(V) sites is too numerous to be totally included, and the long-range disorder is rather difficult to be considered due to the limits in DFT calculations (ab initio calculations for supercells with thousands of atoms should be performed in order to simulate the real case, which is quite difficult to achieve).

3. Preferred doping sites of Cu in bulk amorphous alumina

As it was assumed that under low doping conditions only the preferential coordination sites were occupied, and the local atomic environments of Cu^{2+} at higher doping conditions could often be extracted from progressive loading and preferential site occupations. In order to simulate both the dispersed distribution and aggregated distribution case of Cu doping, the doping of 1, 2, 3, and 4 Cu atoms in 64 Al atoms corresponding to 1.6, 3.2, 4.8, 6.4 at% doping level with varied Cu-Cu distances were all considered, in line with the experimental doping concentrations of the as-synthesized Cu-doped a-Al_2O_3. First we separated the Cu doping from intrinsic defects, ignoring the charge balance, to identify the independent influence of Cu doping and intrinsic defects upon the tuning geometric and electrical properties of amorphous Al_2O_3 systems. Then we studied the cooperation effect of these factors to analyze the possible formation of complex structures consisting of Cu dopants and intrinsic defects. In order to elucidate the difference between the varied Cu doping configurations, we used a simplified tetragonal distorted model to estimate the substitution cost per doped Cu atom. Both the stoichiometric and nonstoichiometric doping schemes were examined: one was simply constructed by replace an Al atom with Cu, the other introduced oxygen vacancy (V_O) around the Cu atom or excess aluminum atom interstitially doped (Al_i) into the former V_{Al} site, to

maintain the electrical neutrality. However, as we discussed above, the charge balance was not a necessary condition for the local charge distribution equilibrium of transition alumina phases, since there were plenty of defects states interacting with each other.

4. The formation energies

The formation energies as a function of $\Delta\mu'_O$ are evaluated according to the formula:

$$E_f(\mu_O) = 1/n_{Cu}E(D) - 1/n_{Cu}E(H) + 1/n_{Cu}[-n_{Cu}\mu_{Cu} + n_{Al}\mu_{Al} + n_O(1/2\mu_{O_2} + \mu_O)] \quad (5)$$

where E(D) is the total energy of the defective cell and E(H) is the total energy of the host cell. n_{Cu} is the number of Cu atoms, n_{Al} is the number of removed Al atoms and n_O is the number of removed oxygen atoms. The chemical potential of bulk metals are used for μ_{Cu} and μ_{Al}. However, this approximation is correct at oxygen poor conditions, and the formation energy is strongly dependent on the reservoirs used to determine the chemical potentials. At higher oxygen concentration, the formation of copper oxides clusters (Cu_2O and CuO) and Al_2O_3 become feasible. Therefore, there are a number of thermodynamic limits to the chemical potentials. To avoid the formation of metallic Cu and molecular O_2, the chemical potential of the atoms in the reservoir must be lower than the elemental reference energies, bounded by

$$\Delta\mu'_{Cu} \leq 0 \qquad \Delta\mu'_O \leq 0 \quad (6)$$

$$2\Delta\mu'_{Cu} + \Delta\mu'_O \leq E_{Cu_2O} \quad \text{(experimental, -1.75 eV)} \quad (7)$$

$$\Delta\mu'_{Cu} + \Delta\mu'_O \leq E_{CuO} \quad \text{(experimental, -1.59 eV)} \quad (8)$$

To avoid the formation of Cu_2O and CuO, the chemical potentials must also be bounded by

$$\Delta\mu'_{Cu} = 0 \quad \text{in the range} \quad -5.2 \leq \Delta\mu'_O \leq -1.75 \quad (9)$$

$$\Delta\mu'_{Cu} = (-1.75 - \Delta\mu'_O)/2 \quad \text{in the range} -1.75 \leq \Delta\mu'_O \leq -1.43 \qquad (10)$$

$$\Delta\mu'_{Cu} = -1.59 - \Delta\mu'_O \quad \text{in the range} \quad -1.43 \leq \Delta\mu'_O \leq 0 \qquad (11)$$

$$\Delta\mu'_{Al} = -5.2 - \Delta\mu'_O \quad \text{for all range of} \quad \Delta\mu'_O \qquad (12)$$

References

1. A. C.-K. Yip, F. L.-Y. Lam, and X. Hu, *Chem. Commun.*, 2005, 3218–3220.

2. M. Anpo, Y. Shioya, H. Yamashita, E. Giamello, C. Morterra, M. Che, H. H. Patterson, S. Webber, and S. Ouellette, *J. Phys. Chem.*, 1994, **98**, 5744–5750.

3. M. Litter, *Appl. Catal. B*, 1999, **23**, 89–114.

4. A. C. Pradhan, B. Nanda, K. M. Parida, and M. Das, *Dalton Trans.*, 2013, **42**, 558–566.

5. K. Wefers, *Aluminum Company of America, 92*, 1987.

6. M. J. Dignam, W. R. Fawcett, and H. Bőhni, *Journal of The Electrochemical Society*, 1966, **113**, 656–662.

7. T. V. Perevalov, O. E. Tereshenko, V. A. Gritsenko, V. A. Pustovarov, A. P. Yelisseyev, C. Park, J. H. Han, and C. Lee, *J. Appl. Phys.*, 2010, **108**, 013501.

8. G. Gutiérrez and B. Johansson, *Phys. Rev. B*, 2002, **65**, 1–9.

9. G. Gutiérrez, E. Menéndez-Proupin, C. Loyola, J. Peralta, and S. Davis, *J. Mater. Chem.*, 2010, **45**, 5124–5134.

10. S. P. Adiga, P. Zapol, and L. A. Curtiss, *Phys. Rev. B*, 2006, **74**, 1–8.

11. H. Momida, S. Nigo, G. Kido, and T. Ohno, *Appl. Phys. Lett.*, 2011, **98**, 042102.

12. C. Boissière, L. Nicole, C. Gervais, F. Babonneau, M. Antonietti, H. Amenitsch, C. Sanchez, and D. Grosso, *Chem. Mater.*, 2006, **18**, 5238–5243.

13. M. Liu and H. Yang, *Colloids Surface. A*, 2010, **371**, 126–130.
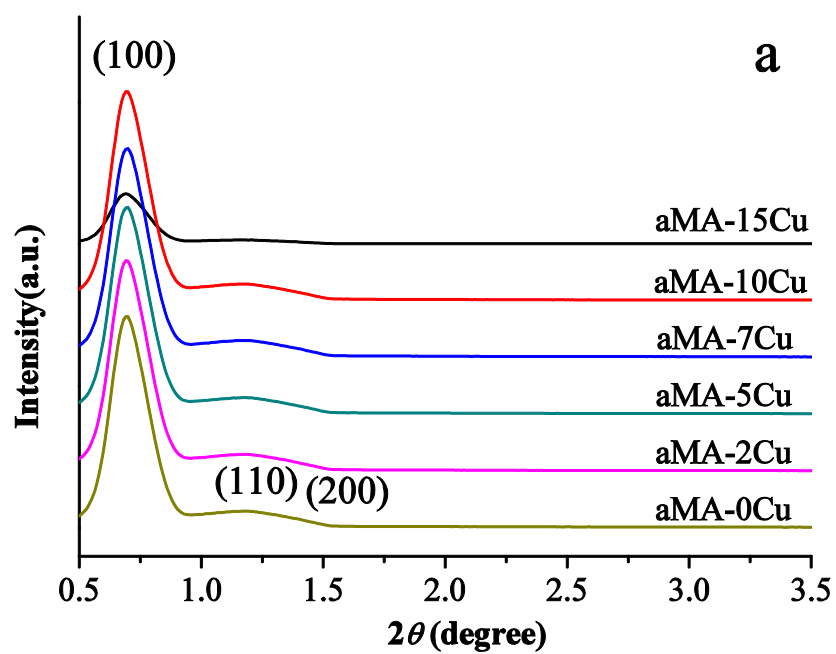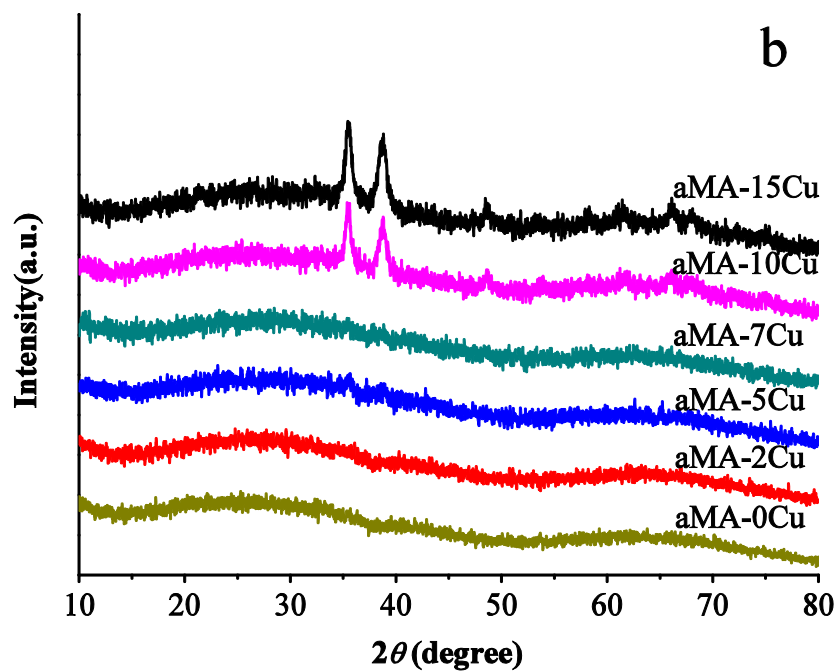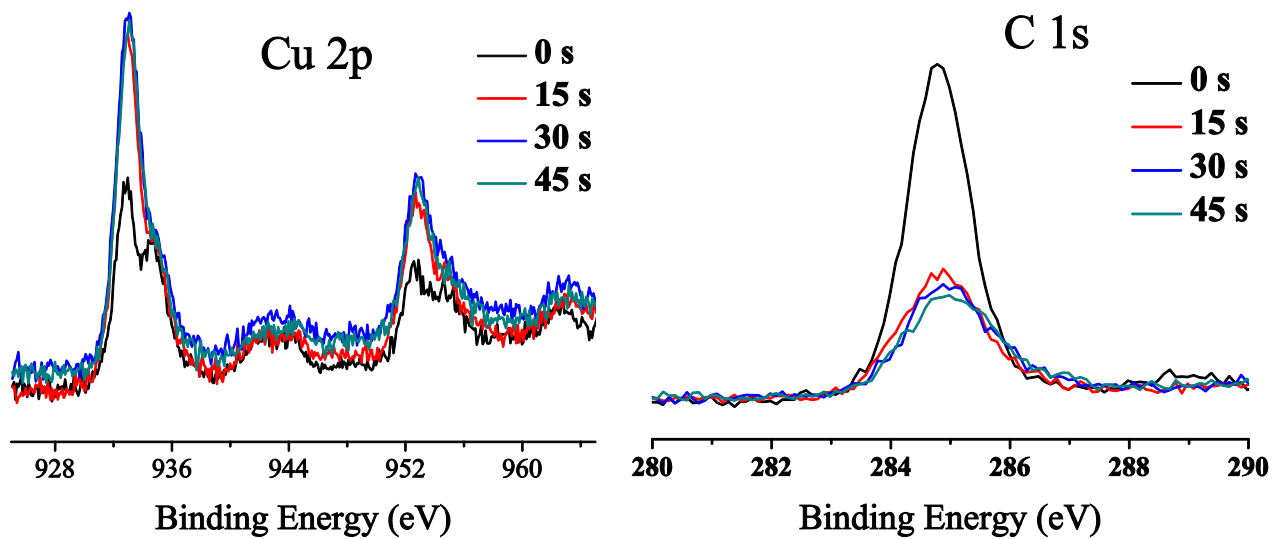
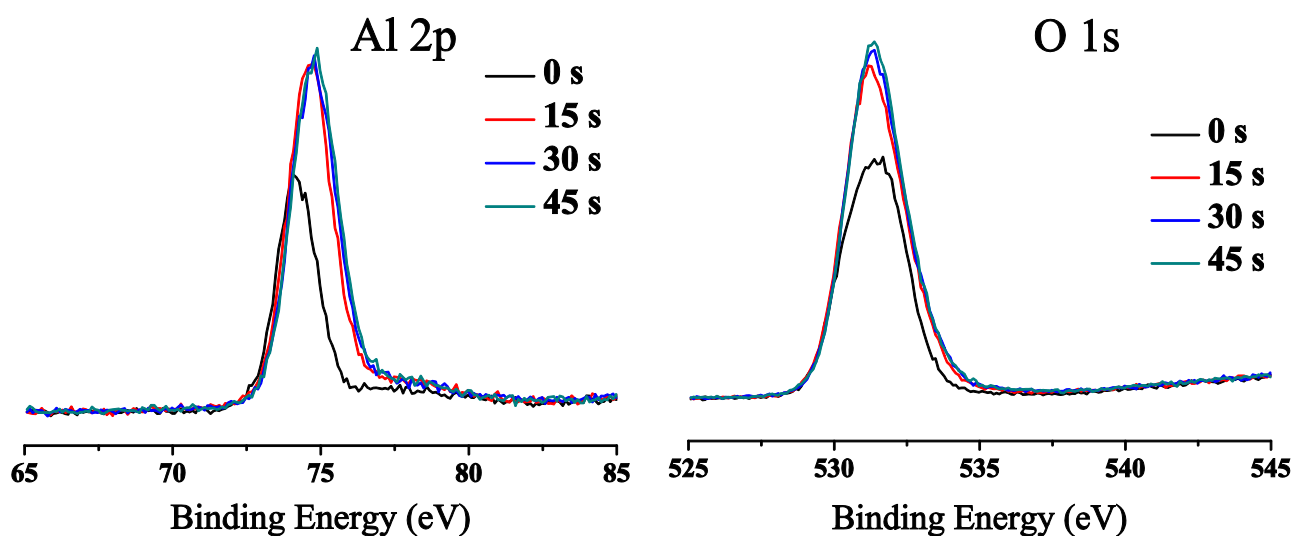**Figure S1**   (A) SAXRD and (B) WAXRD patterns of aMA-xCu samples

Figure S2   XPS depth profiles for aMA-7Cu sample. The C signal was decreased after sputtering,

due to the cleaning of surface-adsorbed hydrocarbons. The weakened signal for Cu, Al, O at 0 s were

originated from the hydroxylated surface structure of Cu-OH, Al-OH. The increase of Cu^+, Al and O

signals and the shift of Al peak to higher value were observed
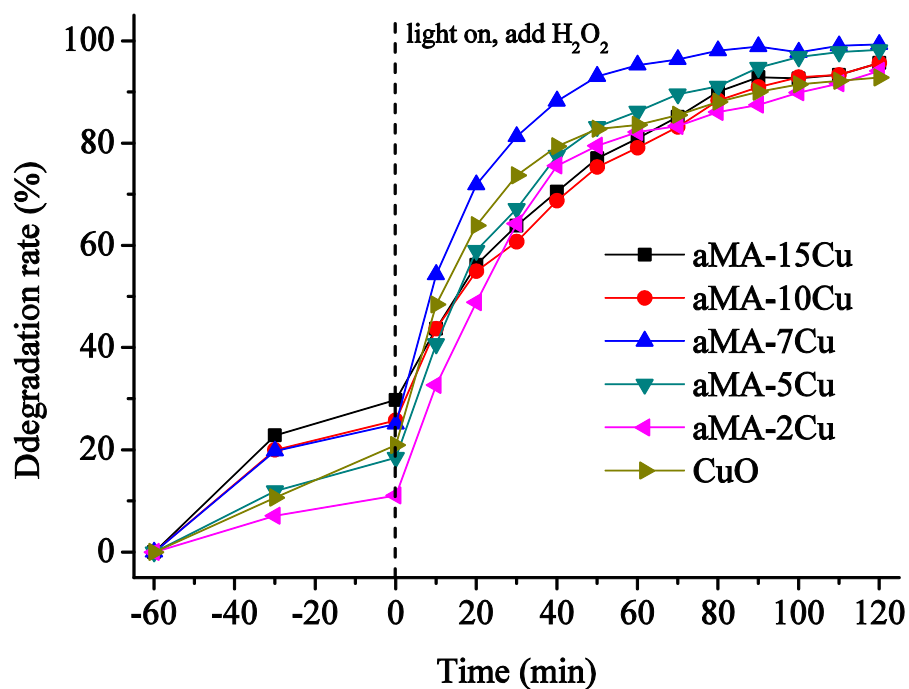
Figure S3   Decolorization efficiency of methyl orange by aMA-xCu samples and commercial

CuO under UV irradiation.
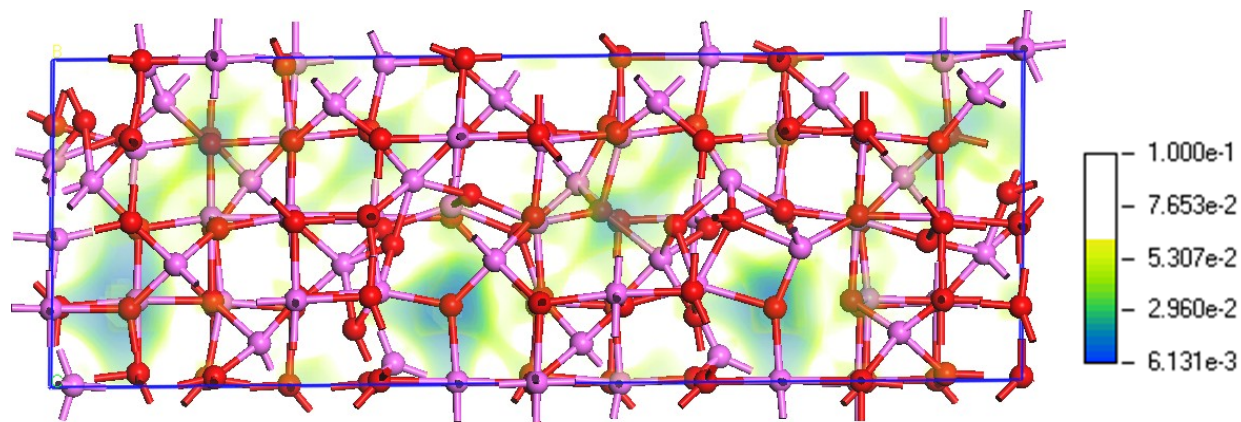
Figure S4   Electron density for the relaxed amorphous Al_2O_3. The contour lines ended at 0.057

$e/Å^3$. The highlighted regions are attributed to oxygen vacancies.
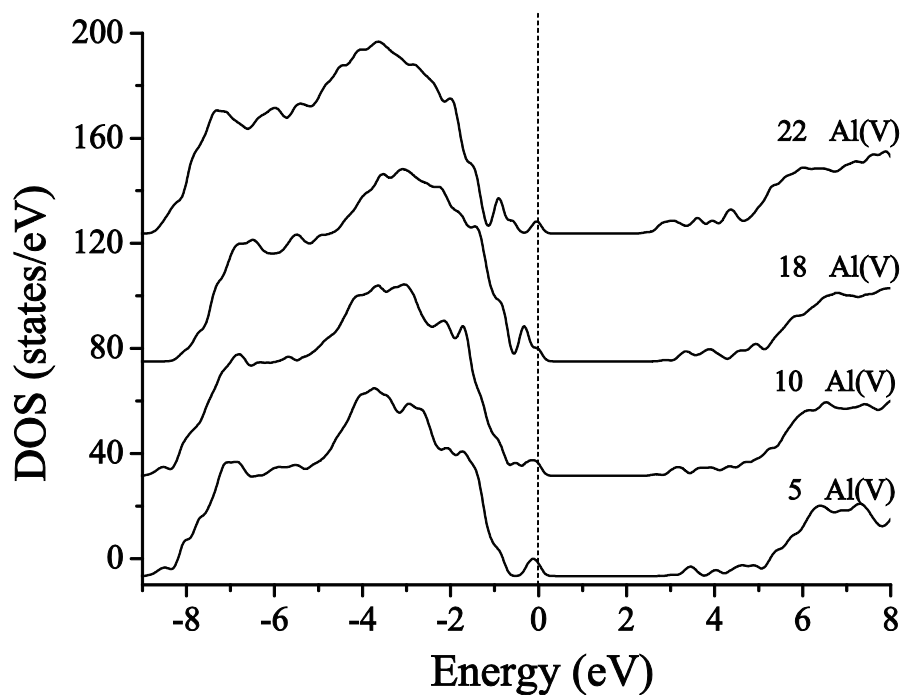
Figure S5 Total density of states (DOS) of amorphous alumina with different degree of distortions.

The degree of distortion is represented by number of Al(V) sites as 5, 10, 18, and 22, respectively.
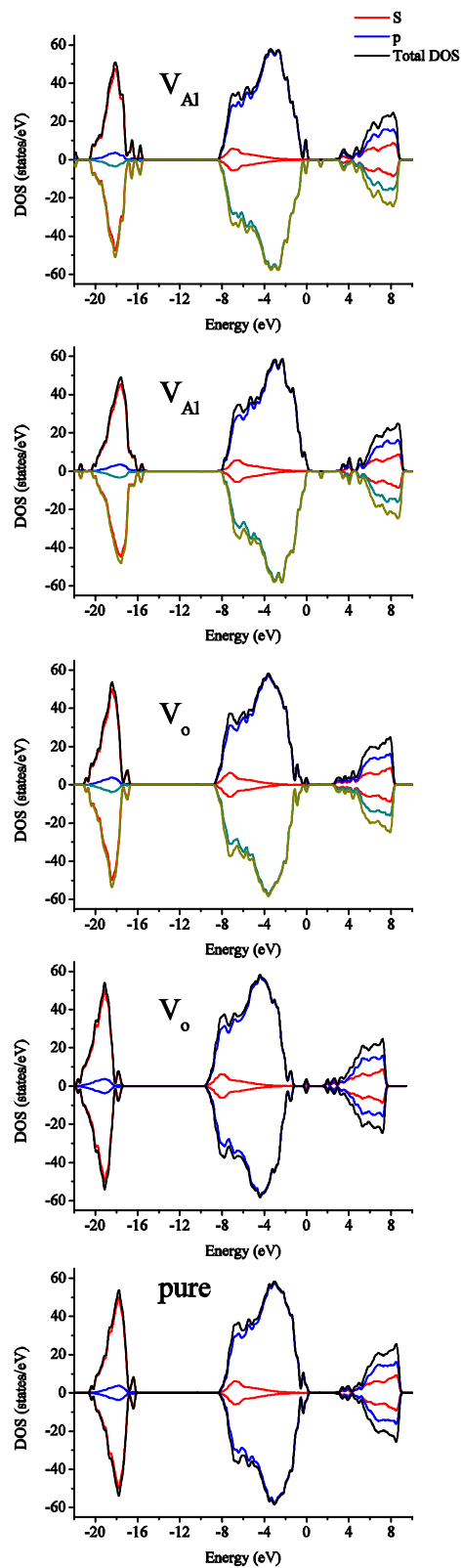
Figure S6 Total density of states (DOS) and atom-projected density of states (PDOS) for PDOS of amorphous Al_2O_3 with or without intrinsic defects V_{Al} or V_O.
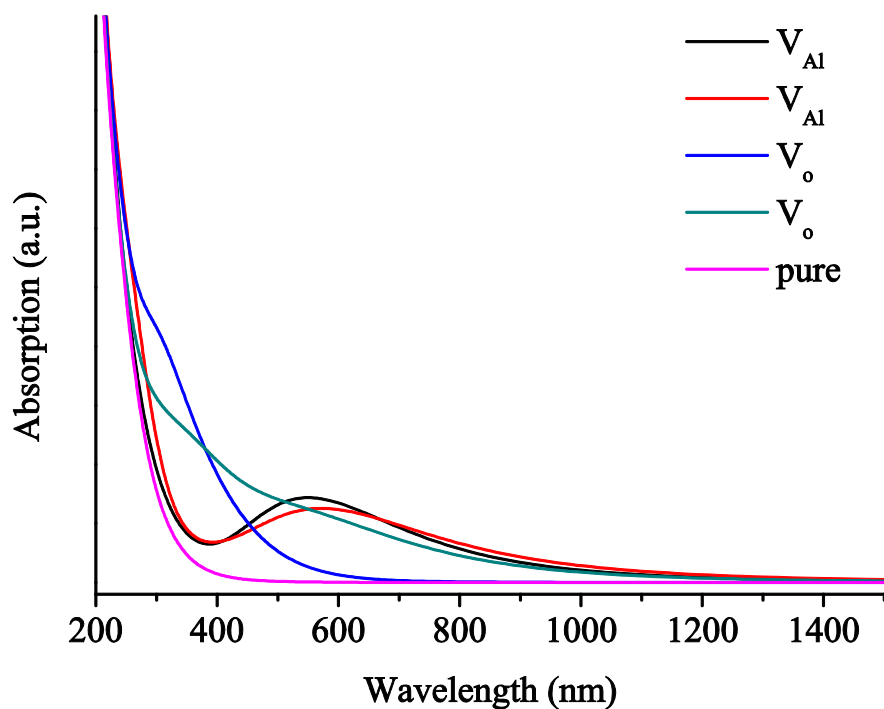
Figure S7. Optical absorption of amorphous Al_2O_3 with intrinsic defects V_{Al} or V_O, corresponding to Figure S6.
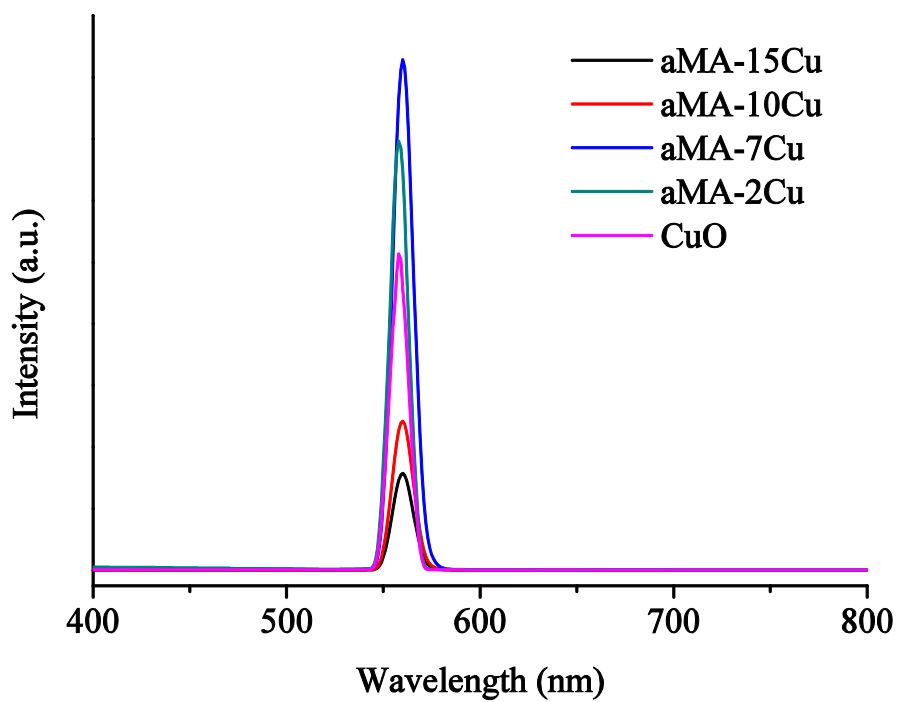
Figure S8. PL spectra of aMA-xCu samples and commercial CuO at room temperature.

14
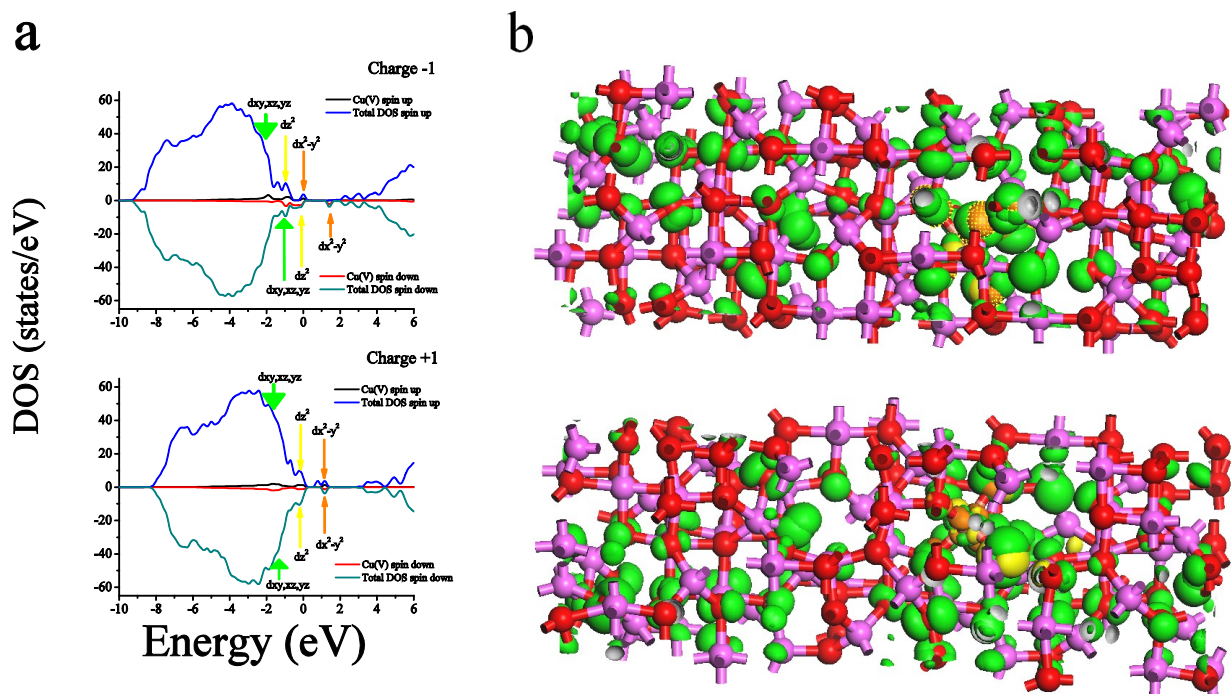
Figure S9 (A) Total density of states (DOS) and atom-projected density of states (PDOS) for Cu^{2+}(V)-doped amorphous Al_2O_3 with charge -1 or charge +1. (B) Partial charge density corresponding to the states pointed by arrows. Each state is shown using the same color. The spin-up orbitals are given.
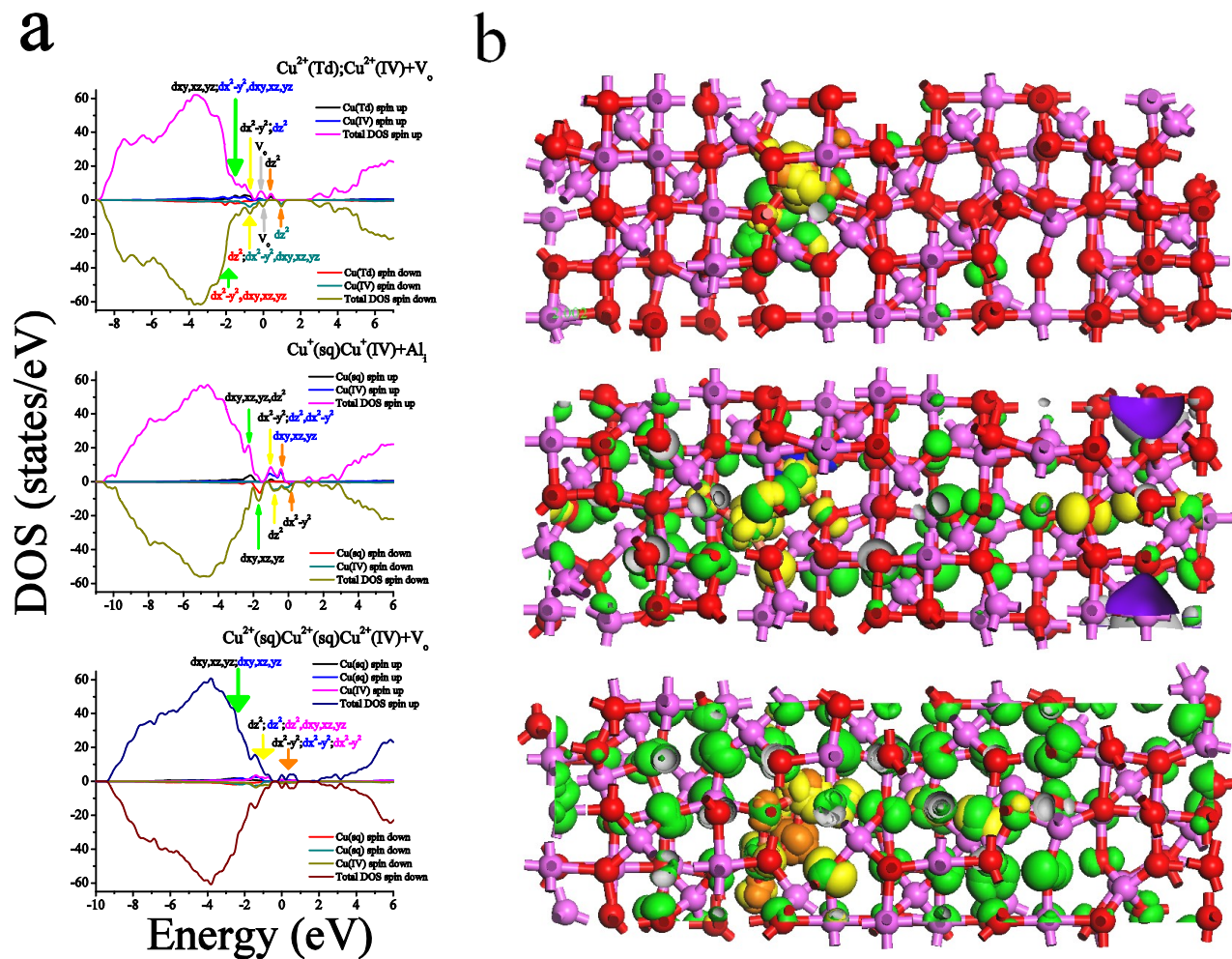
Figure S10 (A) Total density of states (DOS) and atom-projected density of states (PDOS) for PDOS of Cu-doped amorphous Al_2O_3. Three representative aggregated species with intrinsic defects are given as $Cu^{2+}(Td)Cu^{2+}(IV)+V_O$, $Cu^{2+}(sq)Cu^{2+}(IV)+Al_i$ and $Cu^{2+}(sq)Cu^{2+}(sq)Cu^{2+}(IV)+V_O$. (B) Partial charge density corresponding to the states pointed by colored arrows. Each state is shown using the same color. The spin-up orbitals are given.
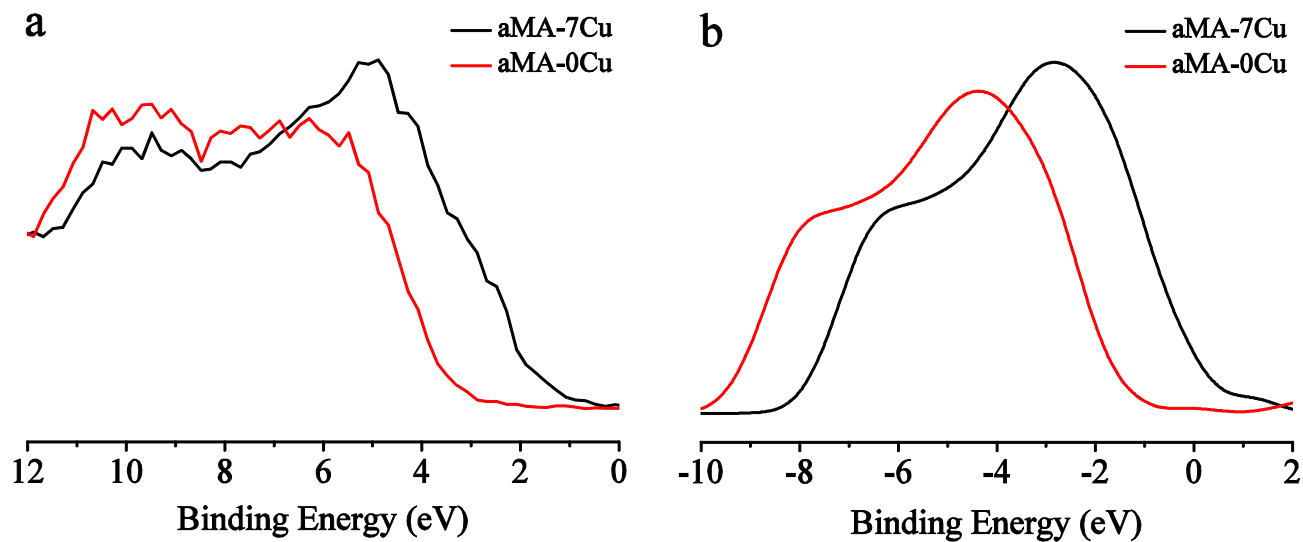
Figure S11. **Comparison of valence band spectra**. (a) the experimental and (b) the calculated values for aMA-7Cu.
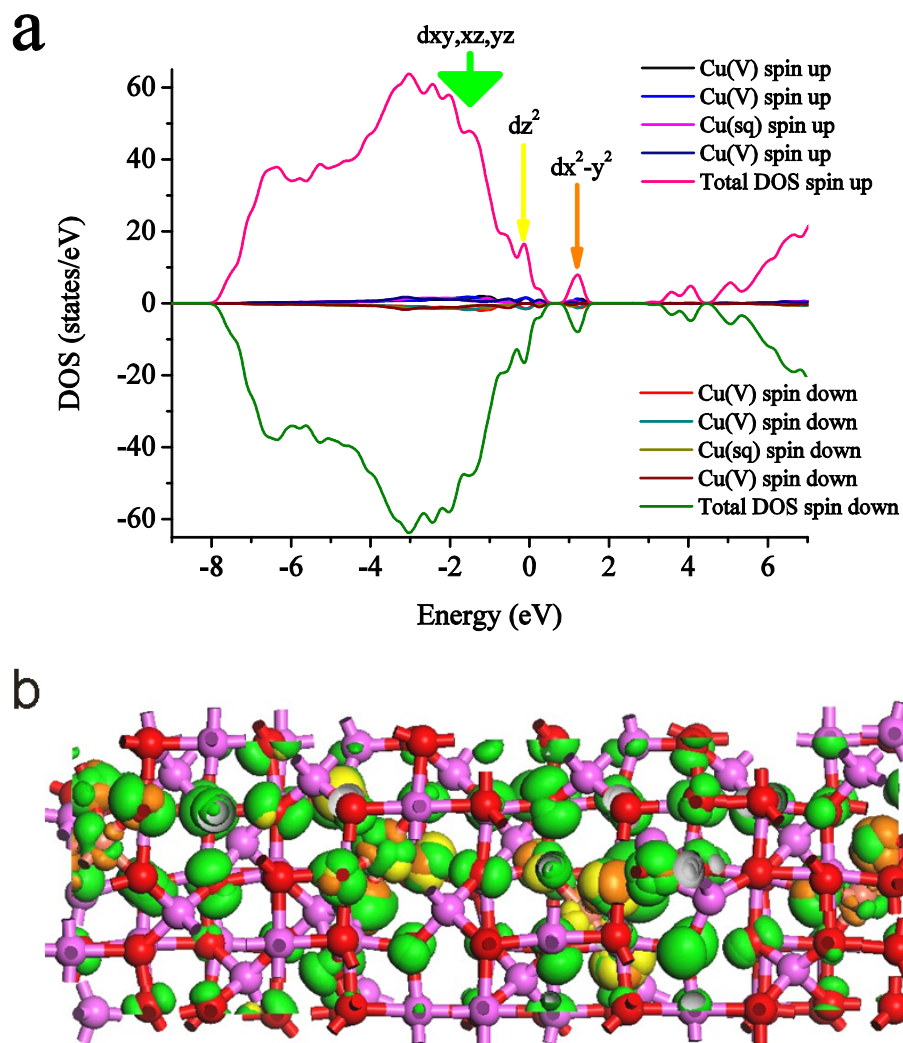
Figure S12 (A) Total density of states (DOS) and atom-projected density of states (PDOS) for PDOS of Cu-doped amorphous Al_2O_3 with four Cu atoms. (B) Partial charge density corresponding to the states pointed by arrows.
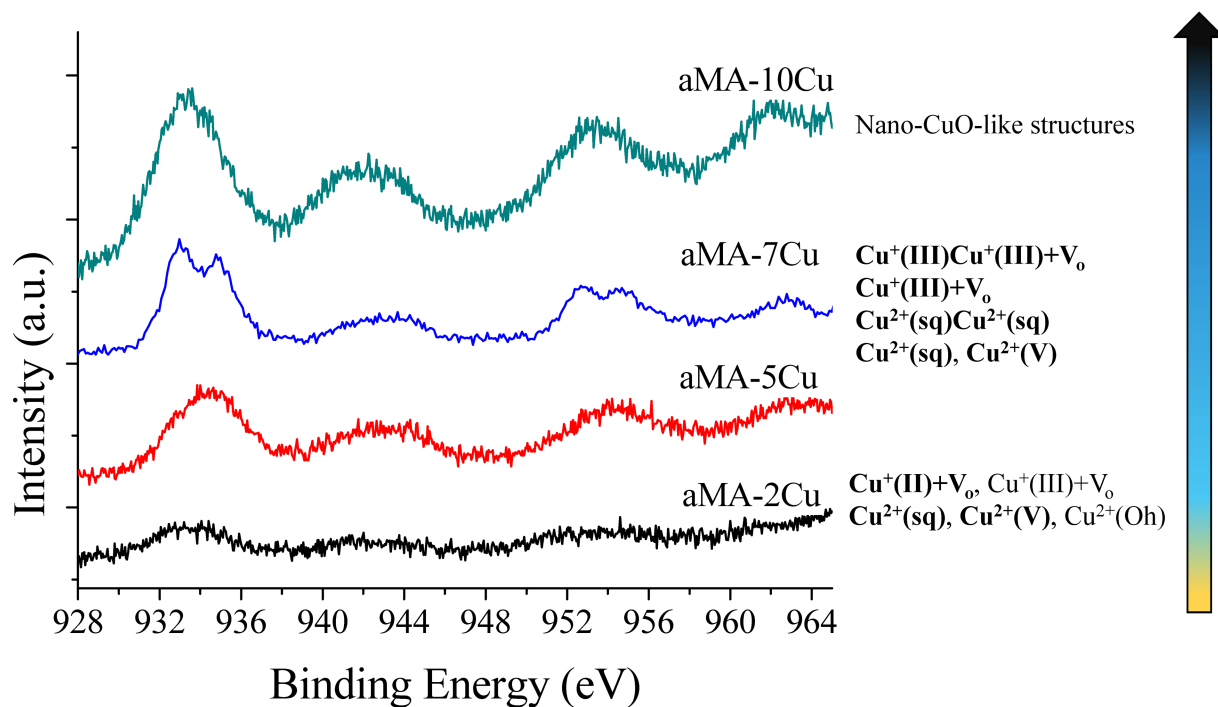
Doping mechanism

Figure S13 The assignment of Cu dopants in amorphous alumina. The dominant Cu species at different doping level are shown on the right. Arrow indicated the variation of sample colors with increase of the copper doping level.